

Article

Structural Design and Analysis of a 100 kW Radial Turbine for an Ocean Thermal Energy Conversion–Organic Rankine Cycle Power Plant

Xin Feng, Haoyang Li, Jie Huang, Qingfen Ma *, Mao Lin, Jingru Li and Zhongye Wu

College of Mechanical and Electrical Engineering, Hainan University, Haikou 570228, China; huangjie@hainanu.edu.cn (J.H.)

* Correspondence: mqf0920@hainanu.edu.cn

Abstract: In this paper, a 100 kW radial inflow turbine is designed for an ocean thermal energy conversion (OTEC) power plant based on the organic Rankine cycle (ORC) with ammonia as the working fluid. Based on one-dimensional (1D) and three-dimensional computational fluid dynamics (3D-CFD) modeling, the mechanical structure design, static and modal analyses of the turbine and its components are carried out to investigate its mechanical performance. The results show the stress and strain distribution in the volute, stator and rotor, and their maximum values appear, respectively, at the inlet cutout, the tip of the stator outlet and the connection position between the rotor and the shaft. After optimization, all the stresses in the above components are below the allowable values. The frequencies from the first order to the sixth order of the rotor and whole turbine were obtained through modal analysis without prestress and under prestress. The maximum frequency of the rotor and whole turbine is 707.75 Hz and 40.22 Hz, both of which are far away from the resonance frequency range that can avoid resonance. Therefore, the structure of the designed turbine is safe, feasible and reliable so as to better guide actual production.



Citation: Feng, X.; Li, H.; Huang, J.; Ma, Q.; Lin, M.; Li, J.; Wu, Z. Structural Design and Analysis of a 100 kW Radial Turbine for an Ocean Thermal Energy Conversion–Organic Rankine Cycle Power Plant. *Processes* **2023**, *11*, 3341. <https://doi.org/10.3390/pr11123341>

Academic Editors: Chia-Nan Wang, Nhat Luong Nhieu, Phan Van-Thanh and Hector Tibo

Received: 28 October 2023
Revised: 18 November 2023
Accepted: 22 November 2023
Published: 30 November 2023



Copyright: © 2023 by the authors. Licensee MDPI, Basel, Switzerland. This article is an open access article distributed under the terms and conditions of the Creative Commons Attribution (CC BY) license (<https://creativecommons.org/licenses/by/4.0/>).

Keywords: ocean thermal energy conversion; radial turbine; static analysis; structural design; modal analysis

1. Introduction

The ocean has a large number of untapped resources, such as ocean thermal energy (OTE), wave energy, tidal energy and water resources [1]. Exploring ocean energy has become an effective way to solve the energy crisis and achieve sustainable development [2]. The ocean is the largest solar energy utilization device on Earth, absorbing solar energy that far exceeds human energy consumption. The Earth receives enough energy from the sun every year to supply its needs [1]. Ocean thermal energy conversion (OTEC) utilizes the temperature difference between warm surface seawater and deep cold seawater as the heat source to realize the utilization of ocean thermal energy [3], possessing the advantages of huge reserves [4], continuous stability, natural cleaning and other characteristics [5,6], with a power generation potential of about 150 million kW [7]. Compared with other ocean clean energy sources, OTE is considered to be the worthiest due to its advantages in terms of high energy density and small power generation fluctuations.

The power generation equipment of an OTEC plant is a turbine, and they can be mainly divided into two categories: axial turbines and radial turbines. Ammonia was the earliest working fluid used and is still the most common in OTEC-ORC systems due to its advantages in terms of its good economy, large unit refrigeration capacity and high heat release coefficient [8–10]. In OTEC systems, the available temperature difference is small [11], limiting the power output and efficiency. Therefore, a radial inflow turbine is generally used in OTEC systems due to its simple structure, good economy, and high efficiency. In order to improve the actual turbine performance under the conditions of low

temperature and pressure, the structural design and optimization of an OTEC radial inflow turbine should be studied.

Some researchers have conducted 1D design [12–15], 3D-CFD simulation [16–18] and other analyses. Nithesh et al. [19] adopted a comprehensive 1D meanline design method for a radial inflow turbine with a 2 kW output power and found that blade edge filleting is very important to improve blade performance. Kim et al. [20] studied and proposed a new method for the appropriate selection of the mass flow rate and loading coefficient and carried out meanline analysis and three-dimensional viscosity simulations in order to verify whether the proposed method can optimize the design of a radial inflow turbine. Nithesh et al. [21] designed a 2 kW radial inflow turbine for OTEC closed-cycle using R22 as the working fluid and conducted a three-dimensional simulation to analyze the importance of blade number and fillet. Wu et al. [22] optimized the design of the dual-pressure steam turbine in the OTEC system based on structural theory. Compared with the initial design point, the total output of the turbine after primary, secondary and third structural optimization increased by 0.69%, 1.82% and 2.02%, respectively. However, these researchers only focused on the analysis and optimization through 3D-CFD simulation for radial turbines, lacking structural design and analysis.

Many scholars have verified the simulation results by conducting experiments. However, their research focused more on building experimental platforms and compared the power output or isentropic efficiency. Structure design analysis and verification for turbines are scarcely carried out. Uusitalo et al. [23] experimentally investigated a small-scale high-temperature ORC, in which the turbine was discovered as having an identical value between the system design value and the mechanical power output of about 6 kW. Weiß et al. [24] designed two small-scale turbines, an axial impulse turbine and a radial cantilever turbine, with a maximum power output of about 12 kW, which had isentropic efficiencies of 73.45% and 76.8%, as experimented on in the ORC test bed. Although the structure and modal analysis [25] of gas turbines can be of significance in terms of reference, the operating conditions of high temperatures and pressures [26] are totally different from those of OTEC-ORC turbines. In addition, the blades of gas turbines are usually made of stainless steel from 12 Cr and Ti-6Al-4V [26], which is not compatible with the working scenarios of OTEC-ORC turbines.

From the above literature investigation, it can be found that the research on turbines mostly focuses on CFD simulation and optimization. There are few studies on the structural design and analysis, especially for OTEC-ORC turbines, which operate at low temperature and pressure and are necessary to meet the efficient, feasible and reliable requirements. Therefore, based on the 1D design and 3D CFD optimization of a 100 kW radial inflow turbine in the OTEC-ORC cycle using ammonia as the working fluid, the mechanical structure and modal analysis as well as stress and strain analysis on the key components and the whole turbine are carried out to ensure the safety, reliability and processability so as to better match the actual production needs and provide guidance for the research of OTEC radial inflow turbines.

2. Aerodynamic Parameter Calculation Based on 1D Design and 3D-CFD Simulation

The meridian plane diagram and the rotor velocity triangles are shown in Figure 1. The 3D-CFD model of the turbine is shown in Figure 2. Mesh software is employed for the volute and diffuser to create tetrahedral mesh, and TurboGrid 19.2 software with ATM (Automatic Topology and Mesh) is used for the nozzle and rotor to create hexahedral mesh with the schematic diagram shown in Figure 3. The number of grid nodes for this design is selected as 1.6×10^6 after a mesh independence test. The calculated thermodynamic and structural parameters are shown in Table 1.

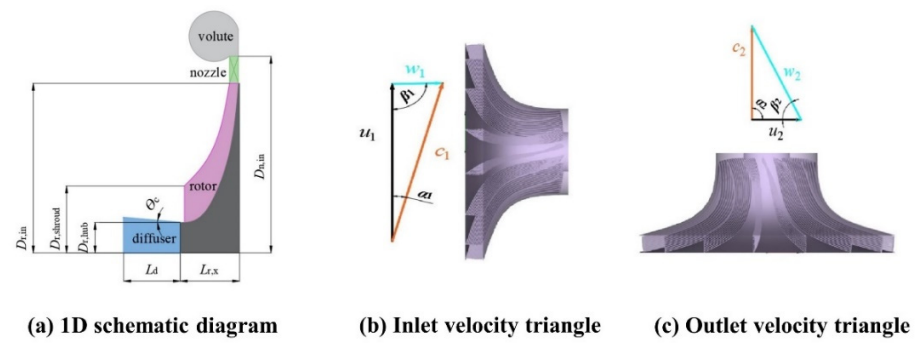


Figure 1. Schematic diagram and rotor velocity triangle of turbine structure.

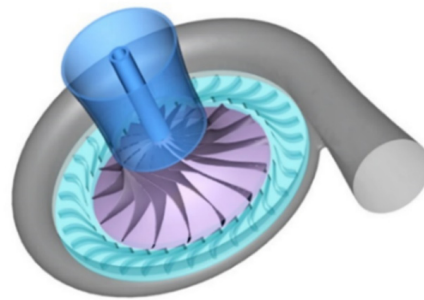
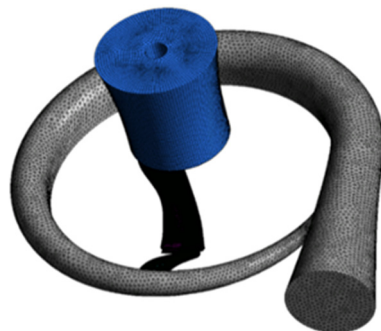


Figure 2. Three-dimensional (3D) model of the designed radial turbine.



(a) Mesh of volute and diffuser.



(b) Mesh of nozzle and rotor.

Figure 3. Mesh diagram.

Steady-state, viscous flow simulation is performed using software CFX. The cubic equation of state by Peng–Robinson is used to calculate the thermodynamic parameters of the expansion process of the working fluid ammonia inside the turbine. Since the Reynolds number of the working fluid in the turbine is much greater than 10^5 , the standard $k-\epsilon$ equation is used to solve the three-dimensional flow problem inside the turbine. The convection scheme of the momentum equation adopts high resolution, and the transport

equation adopts the first order. Because there is no mass transfer or change in chemical composition during the solution process, the energy equation is not considered. The convergence criterion is set as 10^{-6} for the residual target.

Table 1. Main parameters of the designed radial turbine.

Parameters	Units	Value	Parameters	Units	Value
M_{wf}	kg/s	4.09	$D_{r,shroud}$	m	0.208
P	kW	100	ψ	–	0.85
$T_{turb,in}$	°C	24	φ	–	0.95
$p_{turb,in}$	bar	7.3	$D_{n,in}$	mm	476.4
$T_{turb,out}$	°C	11.37	$D_{r,in}$	mm	415.8
$p_{turb,out}$	bar	6.0	$D_{n,out}$	mm	417.8
\bar{D}	–	0.366	$D_{r,shroud}$	mm	209.5
α_1	°	13°	$D_{r,hub}$	mm	48
β_2	°	60°	L_d	mm	257.8
Ω	–	0.437	$L_{r,x}$	mm	145.8
c_{2ss}	m/s	148.01	n	rpm	7000
c_1	m/s	157.79	N_r	–	15
u_1	m/s	153.18	N_n	–	32
w_1	m/s	35.5	$\eta_{t,isen}$	%	89.4
c_2	m/s	32.37	ζ_f	%	4.0%
u_2	m/s	56.06	ζ_1	%	2.0%
w_2	m/s	64.74	ζ_f	%	1.63%

3. Turbine Structural Design

The assembly of the turbine consists of four parts, namely the volute, stator, rotor and diffuser. This section conducts structural design, strength verification, connection and sealing design for these four parts.

3.1. Structural Design of Shaft

Torque is mainly transmitted through shafts when a rotor operates. Fatigue fracture is one of the main failure modes of shafts and tends to occur in places with smaller diameters. When the turbine operates, the main load is torque, and there is no external bending moment. Therefore, only the effect of torque is considered during design and verification.

The torsional strength should meet the requirements of Equation (1) [27].

$$\tau_T = \frac{T}{W_T} = \frac{9.55 \times 10^6 P}{0.2d^3 n} \leq [\tau_T] \quad (1)$$

Wherein, τ_T (MPa), T (N·mm), and W_T (mm^3) are the torsional shear stress, torque on the shaft and torsional section coefficient, respectively. n (rpm), P (kW) and d (mm) are the shaft rotational speed, shaft power and the diameter of the shaft section. $[\tau_T]$ (MPa) is the allowable torsional shear stress.

The allowable torsional shear stress of AISI 1045 steel, the material of the shaft, is 35 MPa [28]. Therefore, the minimum diameter is calculated to be 26.91 mm and then rounded to 30 mm. As shown in Figure 4, a stepped shaft is used in the rotor structure, consisting of diameters of $\Phi 30$, $\Phi 45$, $\Phi 50$, $\Phi 60$, and $\Phi 70$, respectively, and their corresponding lengths are 28 mm, 25 mm, 123 mm, 34 mm, and 60 mm. The ends of the shaft also need to be chamfered to facilitate assembly and deburring.

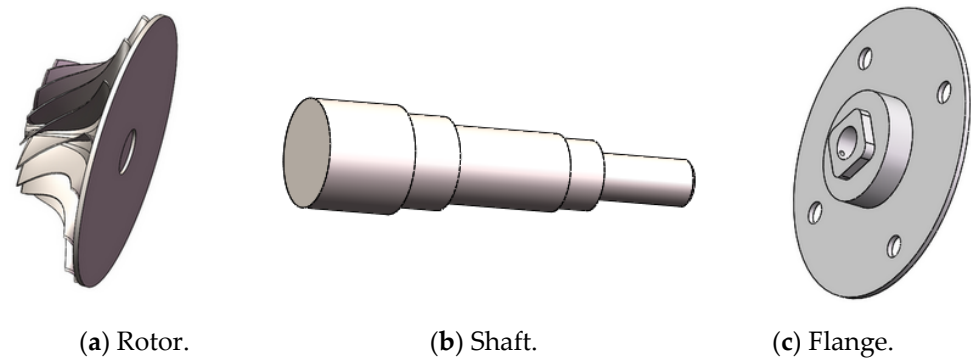


Figure 4. Structure of the shaft and assembled parts.

The torsional stiffness of the shaft is checked according to Equation (2) [27].

$$\varphi_T = 5.73 \times 10^4 \frac{1}{LG} \sum_{i=1}^z \frac{T_i l_i}{I_{pi}} \leq [\varphi_T] \quad (2)$$

$$I_p = \frac{\pi d^4}{32} \quad (3)$$

where φ_T ($^\circ/\text{mm}$), G (MPa) and I_p (mm^4) are the torsion angle, the shear elastic modulus of the shaft material and the polar moment of inertia of the shaft section, respectively. L (mm) is the length of the stepped shaft subjected to torque. T_i , l_i and I_{pi} are the torque, length and polar moment of inertia on the i -th segment of the stepped shaft, respectively. z is the number of shaft segments on which the stepped shaft is subjected to torque. $[\varphi_T]$ ($^\circ/\text{mm}$) is the allowable torsion angle of the circular shaft.

The calculated value of φ_T is $0.0014^\circ/\text{mm}$, less than $0.5^\circ/\text{mm}$, which is the allowable circular shaft torsion angle of the precision transmission shaft. In addition to ensuring the torsional strength and rigidity, the shaft adopts mechanical sealing to effectively ensure the air tightness and achieve long reliable operation.

3.2. Calculation and Selection of the Bearing

As shown in Figure 5, it is a 3D assembly model of the turbine placed vertically. The bearing is required to not only bear radial load but also a certain axial load. Therefore, angular contact ball bearings S7312AC and S7309AC are employed according to the size of the shaft diameter. The contact angles of S7312AC and S7309AC are all 25° , the inner and outer diameters are 60 mm, 45 mm, and 130 mm, 100 mm, respectively, and their widths are 31 mm and 25 mm. The basic dynamic and static load ratings for each are 92.5 kN, 55.1 kN, and 62.6 kN, 37.1 kN. The maximum speeds are 7700 rpm and 10,000 rpm with oil lubrication.

Pitting corrosion damage is a common failure mode of rolling bearings. In order to ensure the effectiveness of the design, the fatigue life of the bearing must be verified. Using high-speed bearings makes the product of the average diameter of the bearing and the rotational speed greater than 0.6×10^6 , which will generate a large amount of heat and can easily cause excessive wear and burns when bearings rotate. Therefore, in addition to ensuring that the bearing has sufficient fatigue life, its limit speed must also be checked to avoid the generation of excessive heat.

The axial force F_{ae} and radial force F_{re} on the shaft can be obtained from Formulas (3) and (4) [28].

$$F_{re} = mg \quad (4)$$

$$F_{ae} = 2T/d \quad (5)$$

$$T = 9.55 \times 10^6 P/n \quad (6)$$

The radial force F_r and the derived axial force F_d on the bearing can be obtained by Formula (7).

$$F_{r1} = \frac{4}{7} F_{re}, F_{r2} = \frac{3}{7} F_{re} \quad (7)$$

$$F_{d1} = 0.68 F_{r1} \quad (8)$$

The axial forces F_{a1} and F_{a2} can be given by Formula (9) and Formula (10), respectively.

$$F_{a2} = F_{d2} \quad (9)$$

$$F_{a1} = F_{ae} - F_{d2} \quad (10)$$

The fatigue life of the bearing can be obtained from Formulas (11) and (12) [29]:

$$L_h = 10^6 \times (C/P)^\varepsilon / 60n \quad (11)$$

$$P = f_p (X F_r + Y F_a) \quad (12)$$

Here, P and C are the equivalent dynamic load and basic dynamic load, respectively. X and Y are the radial and axial dynamic load coefficient, respectively. When $F_a/F_r \leq 0.68$, X and Y take 1 and 0, respectively; otherwise, they take 0.41 and 0.87. f_p is the load coefficient. ε is the life index, and $\varepsilon = 3$ for ball bearings. The life of the bearings selected in this article is much longer than expected and meets the design requirements. Table 2 gives the specific calculation results.

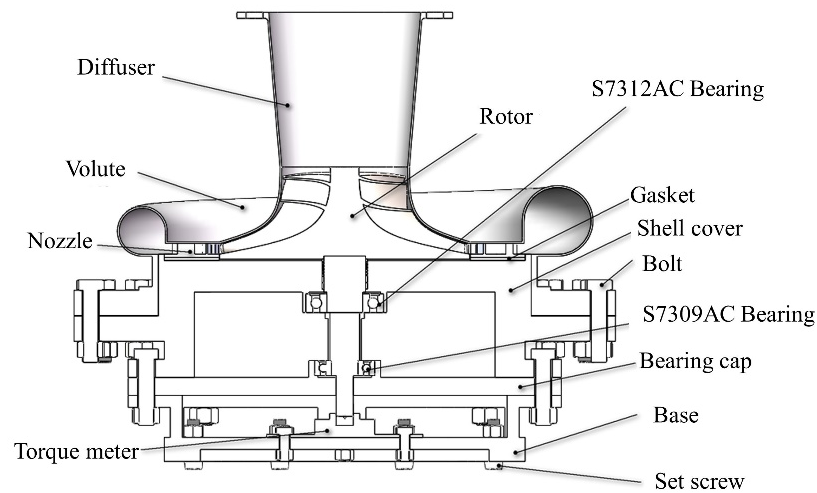


Figure 5. Three-dimensional (3D) structural model of the designed turbine.

Table 2. Bearing force analysis results.

	S7312AC	S7309AC
Radial force (N)	200.73	150.54
Derived axial force (N)	136.49	102.37
Axial force (N)	553.85	102.37
Equivalent dynamic load (N)	620.56	165.59
Bearing life (h)	7.89×10^6	8.77×10^7

In addition to checking the life of the bearing, we should also check the limit speed of the bearing to determine whether the bearing can operate stably. Equation (13) gives

the check condition, which means the maximum speed should be less than or equal to the limit speed:

$$n_{\max} \leq n_{\lim} \quad (13)$$

The bearings adopt oil lubrication in this article. The corresponding limit speeds of the two bearings are 7700 rpm and 10,000 rpm, respectively. The design speed is 7000 rpm, which is smaller than the limit speed of the bearing and meets the requirements.

3.3. Structural Design of Volute and Diffuser

Figure 6 shows the structural model of volute, which makes the working fluid flow axially and symmetrically at the outlet. The connection with the outside is a flange connection. The material of the volute is stainless steel ZG10Cr13. According to GB 150-2011 Pressure Vessels, the wall thickness of volute can be calculated by Formula (14).

$$\delta = \frac{P_t D_v}{2[\sigma]\phi - P_t} \quad (14)$$

where P_t (MPa) and D_v (mm) are the theoretical design pressure and the minimum inner diameter of the volute. ϕ means the welding coefficient, and $[\sigma]$ (MPa) is the allowable stress of the material.

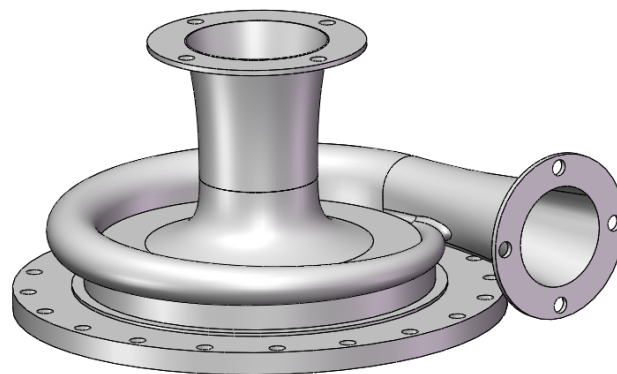


Figure 6. Volute structure diagram.

The equipment is prone to corrosion because of the environment where OTEC is utilized in high humidity and salt. Therefore, the wall thickness of the volute is designed to be 3 mm in this design in order to ensure the normal operation of the equipment.

In addition, the flange is also designed to be welded together with volute, which can facilitate the connection of volute with other components of the turbine. The specific design steps are as follows:

- (1) The maximum working pressure of the designed turbine in this article is 7.3 bar, and the working temperature is 24 °C. Therefore, the nominal pressure is determined to be 1 MPa for safety.
- (2) The type of flange is preliminarily determined to be Type A flat welding based on the above-mentioned parameters. The inner diameter of the volute is 596.4 mm, which is rounded and taken as 600 mm. The corresponding outer diameter of the flange and thickness is 780 mm and 42 mm. The hole diameter and number of the M27 bolt are 30 mm and 20. The outer diameter of the flange and the center diameter of the bolt hole adjust to 900 mm and 845 mm, respectively, in order to avoid the installation.
- (3) The sealing structure is selected as a flat sealing surface, because the working fluid is gaseous ammonia that is not corrosive.
- (4) According to the working temperature, the material of the flange is made of stainless steel ZG10Cr13, which is consistent with the volute material to ensure the uniformity of material, structure, performance and stress during the welding process. The gasket

is made of asbestos rubber, and the material of the stud and nut are AISI 1035 steel and AISI 1025 steel, respectively.

The diffuser discharges the exhaust steam and should have good ability to divert flow. The conical diffuser is utilized in this article. In order to reduce the installation process and reduce the risk of leakage, the diffuser and the volute are integrated into one body, so its thickness and the material are the same as the volute. The outlet of the diffuser is connected with flanges and pipes.

3.4. Structural Design of Stator and Rotor

In the design of the stator, the blades and base are processed separately. The stator blades can be processed by milling and positioned using positioning pins to prevent the stator from rotating. A boss is used to achieve circumferential positioning, and its structure is shown in Figure 7.



Figure 7. Stator structure.

In order to ensure the air tightness of the device, a gasket is utilized for sealing where the blades and the volute base contact. Because the OTEC turbine is operated under low temperature and pressure condition, comparing with the gas turbines operated at high temperature and pressure [25,26], the requirements for the material of an OTEC turbine stator and rotor is less strict, and aluminum alloy 6A04 is selected due to its good processing performance, light weight and high compressive strength. Thus, there is no need for stainless steel from 12Cr and Ti-6Al-4V [26], saving investment cost.

The installation accuracy of the rotor must be guaranteed because it is the key working component. Therefore, a 5 mm deep welding groove is left at the bottom of the rotor to ensure the concentricity between the shaft and rotor. Figure 8 shows a schematic diagram of the connection between the rotor and shaft. The blade thickness of the rotor is 2 mm, and the blade number is 15.

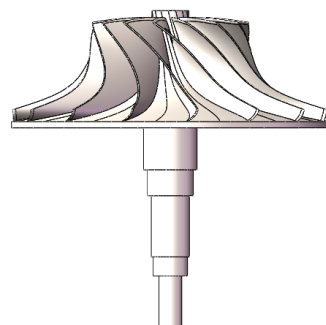


Figure 8. Schematic diagram of rotor and working shaft connection.

4. Structural Strength and Modal Analysis of Turbine

According to the calculation results of CFX, the corresponding constraints and loads are applied. ANSYS 19.2 software is used to analyze the strength of the volute, stator, rotor and shaft. The fluid pressure in the diffuser is low and the velocity is small, so no calibration is required.

4.1. Structural Strength Analysis

First, meshing and independence analysis are performed. Table 3 shows the results of independence analysis; the parameters with italic type are the final grid sizes. The meshing results of the main components are shown in Figure 9.

Table 3. Grid independence analysis.

Volute	Grid Size (mm)			Volute	Deformation (mm)		
	Stator	Rotor	Shaft		Stator	Rotor	Shaft
5	4	8	1	1.373	0.00691	0.0977	0.00296
6	5	10	2	1.238	0.00678	0.0976	0.00295
8	10	11	3	0.886	0.00667	0.0971	0.00295
10	15	15	5	0.607	0.00638	0.0968	0.00293
20	20	20	10	0.197	0.00532	0.0945	0.00296

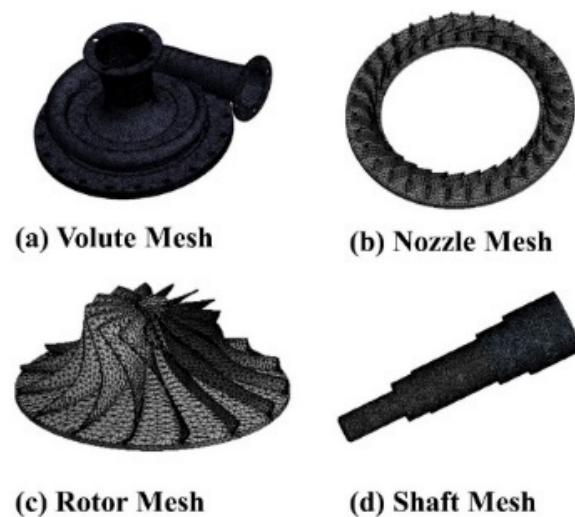


Figure 9. Meshing results of main components.

The stress and strain distribution of the volute are shown in Figure 10a,b. There is a stress concentration at the inlet cut of the volute. The maximum stress of 583 MPa exceeds the maximum allowable stress of the material of 350 MPa, and the maximum strain is 0.00303 mm/mm. Therefore, the volute structure is optimized by adding bosses to make the tip surface more rounded to reduce stress concentration. Figure 10c,d show the optimized stress and strain distribution of the volute. The maximum stress is 124.74 MPa, which meets the design standards. The optimized volute stress is reduced by 78.60%. The strain of the volute is 6.6×10^{-4} mm/mm, which is reduced by 78.22%.

The stator is a stationary component, and the bottom surface is fixedly constrained. Thus, it is mainly affected by gravity, aerodynamic and temperature load. Figure 11 shows the stress and strain distribution of the stator. The maximum stress point appears at the tip of the stationary blade cascade outlet. The maximum stress is 144.72 MPa, half of the material's allowable stress of 280 MPa, which is within the material's bearing capacity. It can be found that part of the blade outlet is more easily deformed than part of the inlet. The deformation is largest at the upper part of the stator blade outlet with a value of 0.0068 mm.

The rotor is the most critical component of the turbine. In this paper, the design speed of the rotor is 7000 rpm. Therefore, in addition to gravity, aerodynamic and temperature load, the inertial force caused by rotation must also be considered. The constraints are the axial constraints on the top end surface and the tangential and normal constraints on the outer diameter cylindrical surface. Figure 12 shows the stress and strain distribution of the rotor, in which we can find that the maximum stress point appears at the connection

between the rotor and shaft. The maximum stress is 100.22 MPa, which is in line with the material’s bearing capacity. In addition, there is also stress concentration at the root of the blade, which can easily cause the blade to break. The maximum strain of the rotor is 0.098 mm, which will occur at the entrance of the rotor because the pressure and inertial force are the largest there.

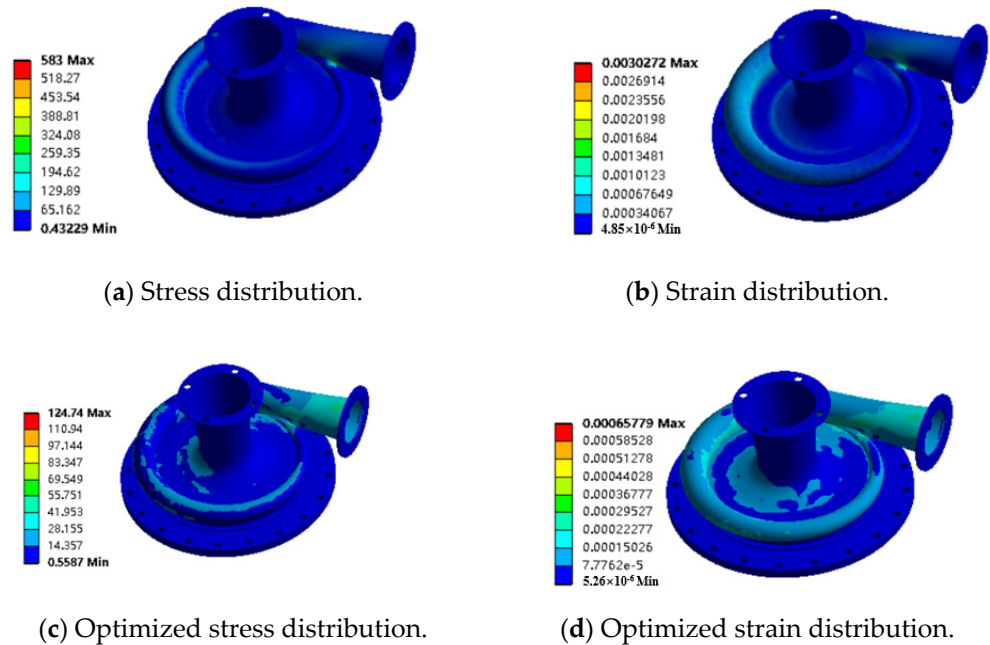


Figure 10. Stress and strain distribution on volute with optimization.

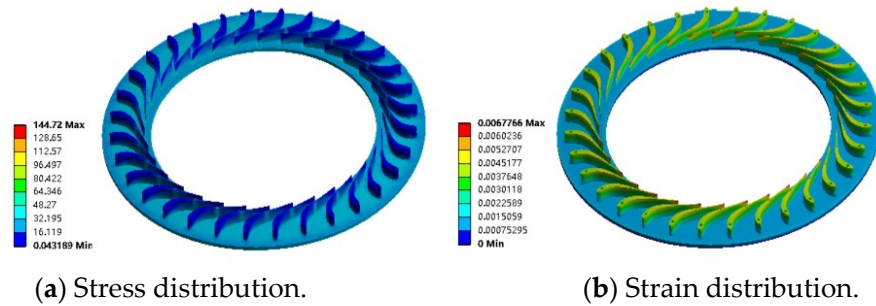


Figure 11. Stress and strain distribution on stator.

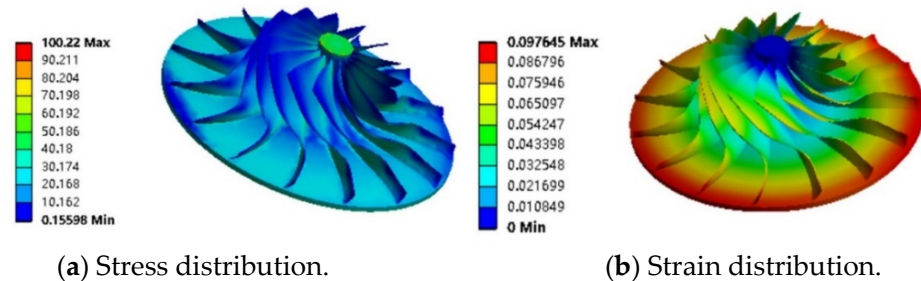


Figure 12. Stress and strain distribution of the rotor.

The shaft is an important component for the turbine to transmit torque, and its strength needs to be checked. The material of the shaft is AISI 1045 steel. Figure 13 shows the strain and stress distribution on the shaft. The maximum stress and strain are 2.946 MPa and 0.0029 mm, respectively, which meet the design requirements.

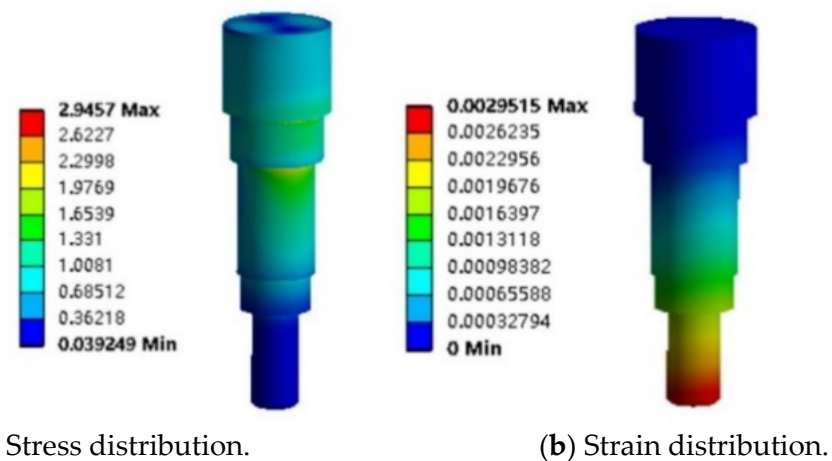


Figure 13. Stress and strain distribution on the shaft.

4.2. Modal Analysis of the Turbine

The movement of rotating parts will inevitably produce vibrations. Through modal analysis, the vibration shape and natural frequency of the rotor can be determined, and the modal parameters in each order of states can be obtained. In addition, the vibration frequency in the assembled state will also be different, so the modal analysis of the complete machine will also be discussed in this section. Modal analysis can be divided into prestressed and non-prestressed states, which will be analyzed and discussed to avoid resonance.

The rotor must bear the effects of loads and constraints during operation, and its vibration frequency will be different from that without prestress. Therefore, the modal analysis under prestress is required. The rotational vibration frequency of the rotor can be obtained through the rotation speed by Formula (15) [30].

$$f = nN/60 \quad (15)$$

Here, n and N are the rotor speed and number of rotor blades, respectively.

If the vibration frequency differs within 15% of the rotational vibration frequency, the object will resonate. The rotational vibration frequency of the rotor in this article is 1750 Hz, and its resonance frequency range is 1487.5–2012.5 Hz

4.2.1. Modal Analysis without Prestress

Modal analysis of the rotor without prestress is performed because the proportion of low-order modal energy in structural vibration is much greater than that of high-order modal energy. The vibration shape diagrams of each order are shown in Figure 14. The vibration frequency of the rotor is 691.25–707.75 Hz. The maximum amplitude appears at the exit of the rotor blade.

When the rotor is running, it will also cause vibration of the turbine; thus, the non-prestressed modal analysis of the whole machine should be performed to ensure that the turbine does not resonate. Figure 15 shows the vibration shape of the radial turbine at each order. The maximum vibration frequency appears at the entrance and exit. Table 4 shows the free mode vibration frequencies of the rotor and turbine. The overall natural vibration frequencies are much smaller than the resonance frequency of the rotor. Therefore, there will be no resonance phenomenon in the rotor and assembly.

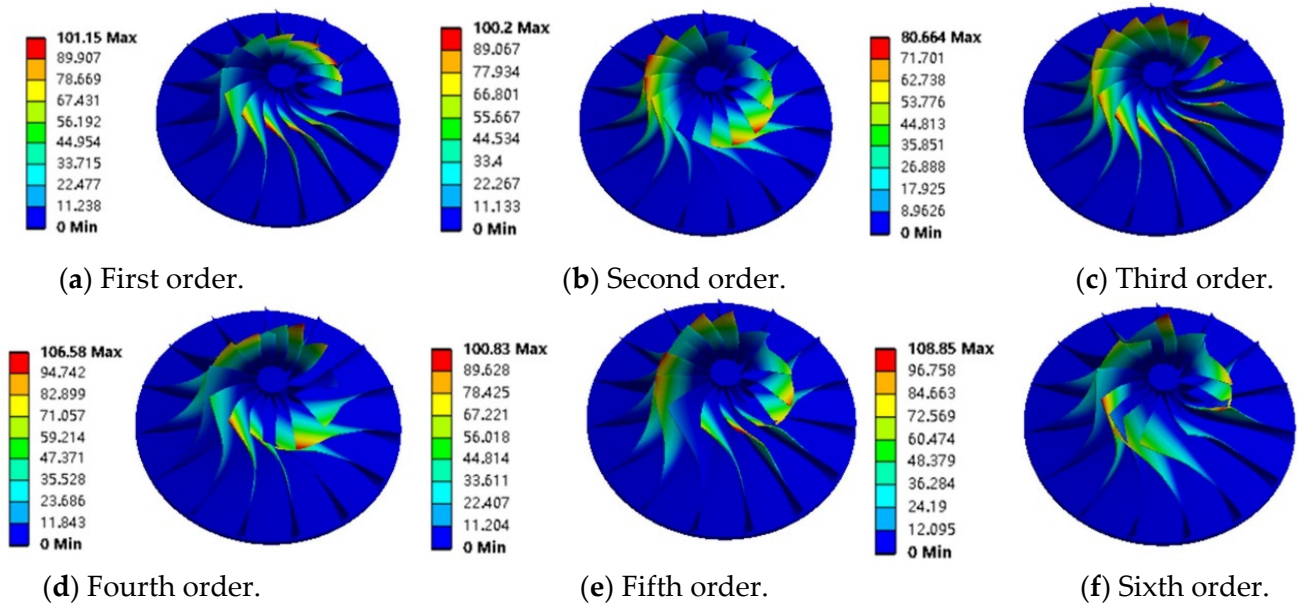


Figure 14. Vibration shapes of the rotor in free mode.

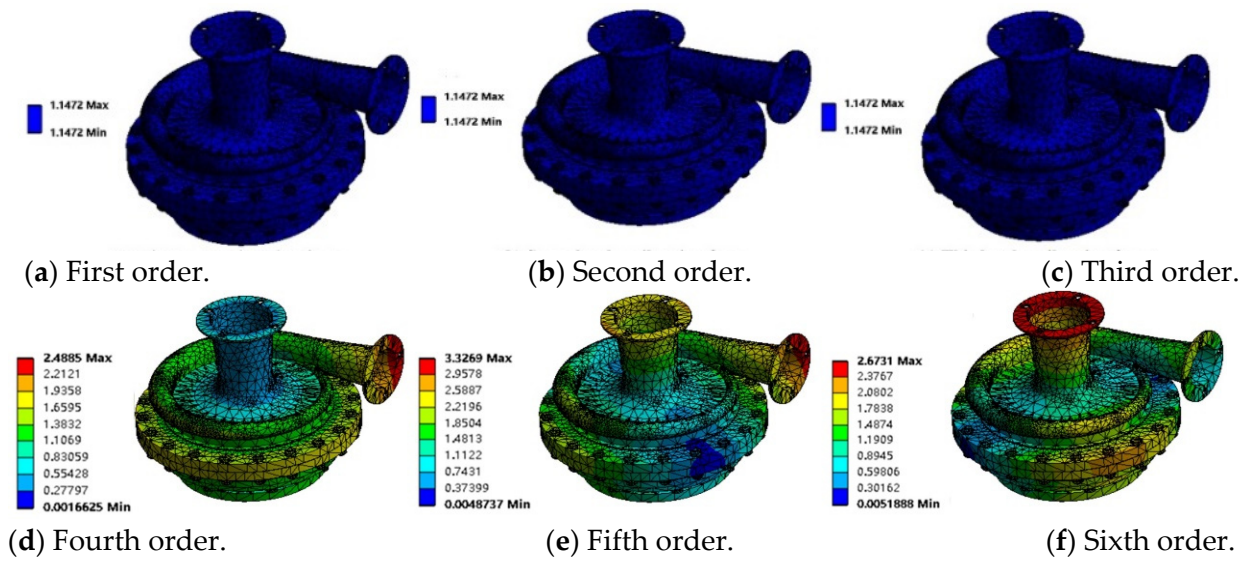


Figure 15. Vibration shapes of the turbine in free mode.

Table 4. Each order frequency of rotor and turbine in free mode.

Orders	Vibration Frequency (Hz)	
	Rotor	Turbine
First order	691.25	0
Second order	691.38	5.00×10^{-4}
Third order	701.55	1.00×10^{-3}
Fourth order	703.98	19.55
Fifth order	704.33	39.68
Sixth order	707.75	40.22

4.2.2. Modal Analysis under Prestress

Each order frequency of the rotor and turbine with prestress is shown in Table 5. Figure 16 presents the vibration shapes. The maximum vibration frequency of the rotor is 721.52 Hz, and its maximum amplitude still appears at the exit of the rotor blade. Compared with the state without prestress, the vibration frequency of the rotor increases slightly, and the rotor does not show obvious stress stiffening. Therefore, it can be considered that the prestress has a small impact on the vibration frequency of the rotor.

Table 5. Each order frequency of rotor and turbine with prestress.

Orders	Vibration Frequency (Hz)	
	Rotor	Turbine
First order	704.22	208.57
Second order	704.35	268.69
Third order	715.14	294.44
Fourth order	717.63	334.01
Fifth order	717.98	348.07
Sixth order	721.52	371.44

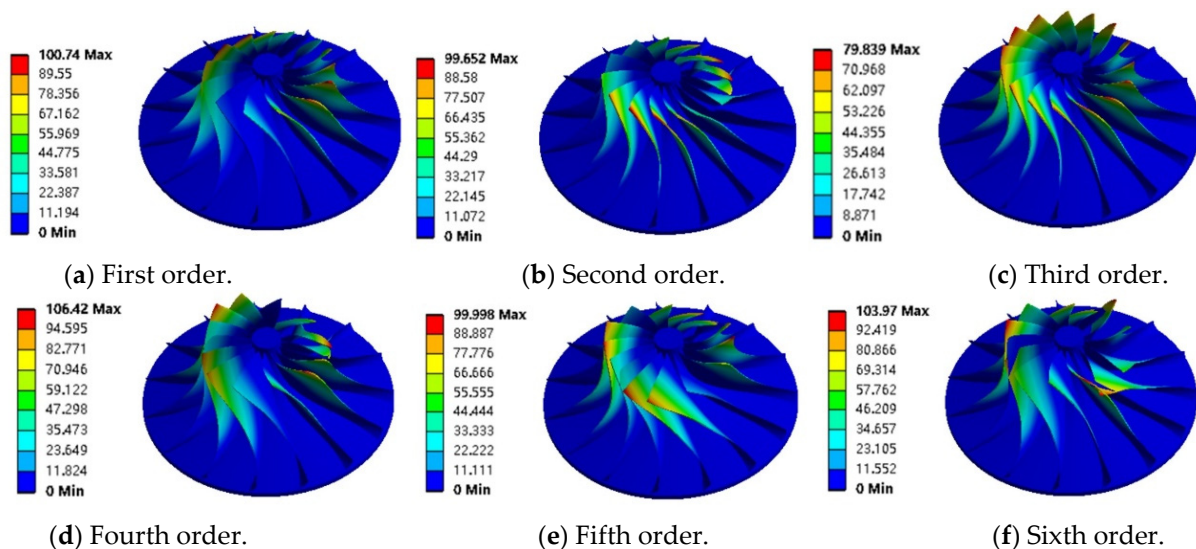


Figure 16. Vibration shapes of the rotor with prestress.

Similarly, the entire turbine should also undergo prestressed modal analysis. The vibration frequency of the six orders with prestress of the overall structure are shown in Table 5. Although the overall vibration frequency is higher than the vibration frequency of the non-prestressed state, it is much smaller than the rotor rotation frequency. Therefore, the resonance of the turbine will not occur. Figure 17 shows the vibration shape of each order of the turbine. Compared with the free mode, in the 2nd, 3rd and 4th orders, the maximum amplitude of the whole machine appears at the exit of the diffuser. In the first and sixth order, the maximum amplitude of the turbine appears at the entrance of the volute.

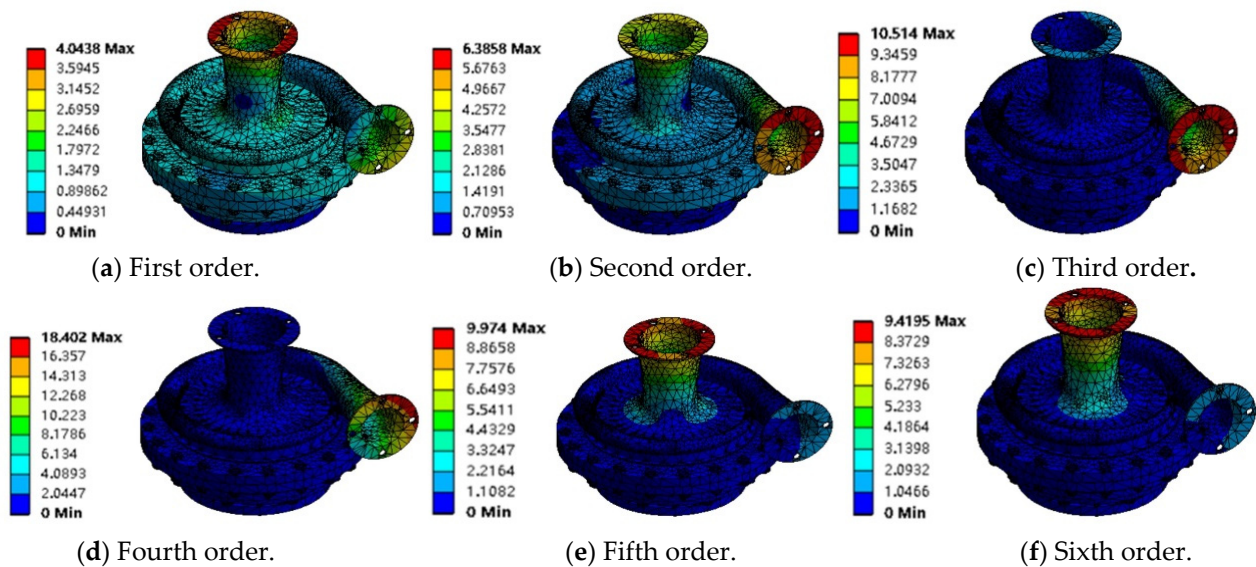


Figure 17. Vibration shapes of the turbine with prestress.

5. Conclusions

A radial inflow turbine is designed for a 100 kW OTEC-ORC plant with ammonia as the working fluid. One-dimensional design and three-dimensional modeling are carried out to obtain thermodynamic and structural parameters of the turbine and key components. To ensure the safety, reliability and processability, structural and modal analysis on the key components, the rotor and the whole turbine are carried out. The results show that the designed structure can meet the requirements.

Through static analysis, the stress and strain distribution on the shaft, volute, stator and rotor are obtained. After optimization, the stress concentration occurs in the volute at the inlet and has the maximum stress with 292.37 MPa, which is lower than the allowable material strength and meets the design requirements. The maximum stress of the stator is 144.72 MPa, which appears at the outlet tip of the blade. The maximum stress of the rotor is 100.22 MPa, which occurs at the connection between the rotor and the shaft. Therefore, from the stress and strain viewpoint, the structural design performed in this paper meets the requirements well.

The frequencies of the rotor and the whole turbine are analyzed by modal analysis without prestress and under prestress, respectively. The maximum frequency of the rotor and whole turbine are 707.75 Hz and 40.23 Hz, which are all far away from the resonance frequency range. Therefore, resonance can be avoided in operation.

The radial turbine designed for OTEC under ambient conditions is efficient with an isentropic efficiency of 89.4%. After conducting mechanical structure and modal analysis, as well as stress and strain analysis on the key components and the equipment as a whole, the safety, reliability and processability of the designed turbine in the OTEC application have been proved, and the results are instructive for researchers and engineers to build an OTEC-ORC turbine prototype and experimental platform.

Although the designed turbine has been proven to be efficient and feasible for the OTEC-ORC by numerical simulation, the prototype may differ with the designed results due to the limitations of manufacturing level, which will influence the performance of the turbine. Furthermore, the turbine is possibly installed on a floating offshore platform; thus, its vibration characteristics will be affected by the movement of the platform, and the coupling effects should be monitored and then considered into the model simulation to optimize the mechanical structure.

Author Contributions: Conceptualization, Supervision, Writing—review and editing, Funding acquisition, Q.M.; Simulation, Data analysis, Writing—original draft, X.F., J.H. and H.L.; Reviewing and supervision, M.L.; Validation and editing, J.L. and Z.W. All authors have read and agreed to the published version of the manuscript.

Funding: This research was funded by the Hainan Provincial Natural Science Foundation of China (422CXTD509), the Hainan Province Science and Technology Special Fund (ZDYF2021GXJS021), and the National Natural Science Foundations of China (51769006).

Data Availability Statement: Data are unavailable due to privacy or ethical restrictions but will be provided when requested.

Conflicts of Interest: The authors declare no conflict of interest.

Nomenclature

c	Absolute speed, m/s	\bar{D}	Ration of wheel diameter
u	Tangential velocity, m/s	Ω	Reaction degree
w	Relative velocity, m/s	ζ	Loss
P	Power, kW	η	Efficiency
m	Mass flow rate, kg/s	τ	Shear stress
n	Rotational speed, rpm	ε	Life index of bearing
Re	Reynolds number	Subscripts	
T	Temperature	turb	Turbine
N	Number	in	Inlet
L	Length, mm	out	Outlet
d	Diameter, mm	1	Rotor inlet
G	Elastic modulus, Mpa	2	Rotor outlet
φ_T	Twist angle, °/mm	r	Rotor
I_p	Polar inertia moment, mm ⁴	n	Nozzle
F	Force, N	r	Radial
X	Radial dynamic load factor	a	Axial
Y	Axial dynamic load factor	u	peripheral
L_h	Bearing life, h	isen	Isentropic
Greek letter		Acronyms	
α	Absolute airflow angle	ORC	Organic Rankine Cycle
β	Relative airflow angle	OTEC	Ocean Thermal Energy Conversion
χ	Characteristic ratio	CFD	Computational fluid dynamics
ϕ	Nozzle velocity coefficient	1-D	One-dimensional
ψ	Rotor velocity coefficient	3-D	Three-dimensional

References

- Khan, N.; Kalair, A.; Abas, N.; Haider, A. Review of ocean tidal, wave and thermal energy technologies. *Renew. Sustain. Energy Rev.* **2017**, *72*, 590–604. [\[CrossRef\]](#)
- Hasan, A.; Dincer, I. A new integrated ocean thermal energy conversion-based trigeneration system for sustainable communities. *J. Energy Resour. Technol.* **2020**, *142*, 061301. [\[CrossRef\]](#)
- Sun, F.; Ikegami, Y.; Jia, B.; Arima, H. Optimization design and exergy analysis of organic rankine cycle in ocean thermal energy conversion. *Appl. Ocean Res.* **2012**, *35*, 38–46. [\[CrossRef\]](#)
- Hasan, A.; Dincer, I. An ocean thermal energy conversion based system for district cooling, ammonia and power production. *Int. J. Hydrogen Energy* **2020**, *45*, 15878–15887. [\[CrossRef\]](#)
- Matsuda, Y.; Oouchida, R.; Sugi, T.; Goto, S.; Yasunaga, T.; Ikegami, Y. Power generation control of OTEC plant using double-stage Rankine cycle with target power output variation by simultaneous regulation of multiple flow rates. In Proceedings of the 2019 58th Annual Conference of the Society of Instrument and Control Engineers of Japan (SICE), Hiroshima, Japan, 10–13 September 2019; pp. 1412–1417.
- Hernández-Romero, I.M.; Nápoles-Rivera, F.; Flores-Tlacuahuac, A.; Fuentes-Cortés, L.F. Optimal design of the ocean thermal energy conversion systems involving weather and energy demand variations. *Chem. Eng. Process.-Process Intensif.* **2020**, *157*, 108114. [\[CrossRef\]](#)
- Dongna, M. Overview of ocean energy power generation. *Sci. Technol. Inf.* **2015**, *13*, 246–247.
- Yoon, J.-I.; Son, C.-H.; Baek, S.-M.; Ye, B.H.; Kim, H.-J.; Lee, H.-S. Performance characteristics of a high-efficiency R717 OTEC power cycle. *Appl. Therm. Eng.* **2014**, *72*, 304–308. [\[CrossRef\]](#)

9. Mohd Idrus, N.H.; Musa, M.N.; Yahya, W.J.; Ithnin, A.M. Geo-Ocean Thermal Energy Conversion (GeOTEC) power cycle/plant. *Renew. Energy* **2017**, *111*, 372–380. [[CrossRef](#)]
10. Zhang, C.; Wu, Z.; Wang, J.; Ding, C.; Gao, T.; Chen, Y. Thermodynamic performance of a radial-inflow turbine for ocean thermal energy conversion using ammonia. *Renew. Energy* **2023**, *202*, 907–920. [[CrossRef](#)]
11. Liu, W.; Xu, X.; Chen, F.; Liu, Y.; Li, S.; Liu, L.; Chen, Y. A review of research on the closed thermodynamic cycles of ocean thermal energy conversion. *Renew. Sustain. Energy Rev.* **2020**, *119*, 109581. [[CrossRef](#)]
12. Alshammari, F.; Khedher, N.B.; Said, L.B. Development of an automated design and off-design radial turbine model for solar organic Rankine cycle coupled to a parabolic trough solar collector. *Appl. Therm. Eng.* **2023**, *230*, 120677. [[CrossRef](#)]
13. Xu, G.; Zhao, G.; Quan, Y.; Liang, R.; Li, T.; Dong, B.; Fu, J. Design and optimization of a radial-axial two-stage coaxial turbine for high-temperature supercritical organic Rankine cycle. *Appl. Therm. Eng.* **2023**, *227*, 120365. [[CrossRef](#)]
14. Yu, Z.; Wang, C.; Rong, F.; Liang, W. Optimal coupling design for organic Rankine cycle and radial turbine rotor using CFD modeling, machine learning and genetic algorithm. *Energy Convers. Manag.* **2023**, *275*, 116493. [[CrossRef](#)]
15. Ma, Q.; Gao, Z.; Huang, J.; Mahian, O.; Feng, X.; Lu, H.; Wang, S.; Wang, C.; Tang, R.; Li, J. Thermodynamic analysis and turbine design of a 100 kW OTEC-ORC with binary non-azeotropic working fluid. *Energy* **2023**, *263*, 126097. [[CrossRef](#)]
16. Uusitalo, A.; Zocca, M. Design and numerical analysis of supersonic radial-inflow turbines for transcritical ORC processes. *Energy Convers. Manag.* **2023**, *277*, 116609. [[CrossRef](#)]
17. Li, W.; Ni, Q.; Ling, X. Investigations on ORC radial inflow turbine three-dimensional geometry design and off-design performance prediction. *Case Stud. Therm. Eng.* **2023**, *44*, 102893. [[CrossRef](#)]
18. Gunawan, G.; Permana, D.I.; Soetikno, P. Design and numerical simulation of radial inflow turbine of the regenerative Brayton cycle using supercritical carbon dioxide. *Results Eng.* **2023**, *17*, 100931. [[CrossRef](#)]
19. Nithesh, K.G.; Chatterjee, D. Numerical prediction of the performance of radial inflow turbine designed for ocean thermal energy conversion system. *Appl. Energy* **2016**, *167*, 1–16. [[CrossRef](#)]
20. Kim, N.J.; Ng, K.C.; Chun, W. Using the condenser effluent from a nuclear power plant for Ocean Thermal Energy Conversion (OTEC). *Int. Commun. Heat Mass Transf.* **2009**, *36*, 1008–1013. [[CrossRef](#)]
21. Nithesh, K.G.; Chatterjee, D.; Oh, C.; Lee, Y.-H. Design and performance analysis of radial-inflow turboexpander for OTEC application. *Renew. Energy* **2016**, *85*, 834–843. [[CrossRef](#)]
22. Wu, Z.; Feng, H.; Chen, L.; Xie, Z.; Cai, C.; Xia, S. Optimal design of dual-pressure turbine in OTEC system based on constructal theory. *Energy Convers. Manag.* **2019**, *201*, 112179. [[CrossRef](#)]
23. Uusitalo, A.; Turunen-Saaresti, T.; Honkatukia, J.; Dhanasegaran, R. Experimental study of small scale and high expansion ratio ORC for recovering high temperature waste heat. *Energy* **2020**, *208*, 118321. [[CrossRef](#)]
24. Weiß, A.P.; Popp, T.; Müller, J.; Hauer, J.; Brüggemann, D.; Preißinger, M. Experimental characterization and comparison of an axial and a cantilever micro-turbine for small-scale Organic Rankine Cycle. *Appl. Therm. Eng.* **2018**, *140*, 235–244. [[CrossRef](#)]
25. Xu, M.; Cao, L.; Song, L. Structure and modal analysis of the last stage blade in steam turbine under low volume flow conditions. *Eng. Fail. Anal.* **2022**, *131*, 105820. [[CrossRef](#)]
26. Zhu, M. Design and analysis of steam turbine blades. *J. Phys. Conf. Ser.* **2019**, *1300*, 012056. [[CrossRef](#)]
27. Paul, S.; Charles, C. *Torsional Analysis of Structural Steel Members*; American Institute of Steel Construction: Chicago, IL, USA, 1997.
28. Lianggui, P. *Mechanical Design*, 9th ed.; Higher Education Press: Beijing, China, 2013; pp. 303–332.
29. Hua, Z. Analysis of the Support Structure of 60° Angular Contact Ball Bearings for Ball Screws. *Mech. Manag. Dev.* **2023**, *38*, 8–9. [[CrossRef](#)]
30. Jie, X. Modal analysis of local ventilator impeller for mining based on ANSYS. *Technol. Innov. Appl.* **2016**, *31*, 65.

Disclaimer/Publisher’s Note: The statements, opinions and data contained in all publications are solely those of the individual author(s) and contributor(s) and not of MDPI and/or the editor(s). MDPI and/or the editor(s) disclaim responsibility for any injury to people or property resulting from any ideas, methods, instructions or products referred to in the content.